STABILITY OF CO₂ ATMOSPHERES ON DESICCATED M DWARF EXOPLANETS

PETER GAO[1,2], RENYU HU[1,3,6], TYLER D. ROBINSON[4,5,7], CHENG LI[1], AND YUK L. YUNG[1]
[1] Division of Geological and Planetary Sciences, California Institute of Technology, Pasadena, CA 91125, USA; pgao@caltech.edu
[2] NASA Astrobiology Institute's Virtual Planetary Laboratory, Seattle, WA 98195, USA
[3] Jet Propulsion Laboratory, California Institute of Technology, Pasadena, CA 91109, USA
[4] Ames Research Center, Mountain View, CA 94035, USA
[5] Oak Ridge Associated Universities Oak Ridge, TN 37830, USA

ABSTRACT

We investigate the chemical stability of CO_2-dominated atmospheres of desiccated M dwarf terrestrial exoplanets using a one-dimensional photochemical model. Around Sun-like stars, CO_2 photolysis by Far-UV (FUV) radiation is balanced by recombination reactions that depend on water abundance. Planets orbiting M dwarf stars experience more FUV radiation, and could be depleted in water due to M dwarfs' prolonged, high-luminosity pre-main sequences. We show that, for water-depleted M dwarf terrestrial planets, a catalytic cycle relying on H_2O_2 photolysis can maintain a CO_2 atmosphere. However, this cycle breaks down for atmospheric hydrogen mixing ratios <1 ppm, resulting in ~40% of the atmospheric CO_2 being converted to CO and O_2 on a timescale of 1 Myr. The increased O_2 abundance leads to high O_3 concentrations, the photolysis of which forms another CO_2-regenerating catalytic cycle. For atmospheres with <0.1 ppm hydrogen, CO_2 is produced directly from the recombination of CO and O. These catalytic cycles place an upper limit of ~50% on the amount of CO_2 that can be destroyed via photolysis, which is enough to generate Earth-like abundances of (abiotic) O_2 and O_3. The conditions that lead to such high oxygen levels could be widespread on planets in the habitable zones of M dwarfs. Discrimination between biological and abiotic O_2 and O_3 in this case can perhaps be accomplished by noting the lack of water features in the reflectance and emission spectra of these planets, which necessitates observations at wavelengths longer than 0.95 μm.

Key words: planets and satellites: atmospheres – planets and satellites: physical evolution – planets and satellites: terrestrial planets

1. INTRODUCTION

M dwarfs are prime targets for the detection and characterization of terrestrial exoplanets by the *James Webb Space Telescope (JWST)*, as they are abundant in the solar neighborhood and their small radii allow for greater transit signals from Earth-sized exoplanets (e.g., Quintana et al. 2014). As a result, terrestrial exoplanets in orbit of M dwarfs may offer the best opportunities for the detection of biosignatures in the near future, such as O_2 and O_3. However, these species are also produced by CO_2 photolysis, leading to potential false positives in biosignature detection. Previous studies have shown that low H_2O, high CO_2 atmospheres tend to generate more O_2 and O_3, though the conclusions are very sensitive to surface boundary conditions and atmospheric escape rates (Selsis et al. 2002; Segura et al. 2007; Zahnle et al. 2008; Hu et al. 2012; Domagal-Goldman et al. 2014; Tian et al. 2014).
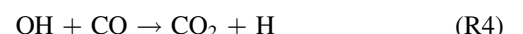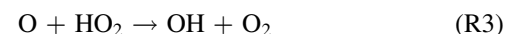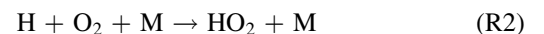
Recent works by Luger & Barnes (2015) and Tian & Ida (2015) have shown that M dwarf terrestrial exoplanets may be severely depleted in water relative to Earth. Prior to the main sequence, M dwarfs evolve along the Hayashi Track for 100 Myr–1 Gyr with much higher luminosities than later in their evolution (Hayashi 1961). Therefore, any planets in the habitable zone of a main sequence M dwarf would experience a prolonged period of high insolation before the main sequence, leading to a Runaway Greenhouse phase and the loss of much of their atmospheric and surficial water. Their crust and upper

mantle could also become desiccated if a surface magma ocean forms as a result of the Runaway Greenhouse, in which case they could be heavily oxidized by acting as a sink for the excess oxygen generated by water photolysis and hydrogen escape (Luger & Barnes 2015). Such planets would be vastly different from Earth in terms of atmospheric chemistry and subsequent evolution. For example, the low atmospheric water content, whether as a result of the initial global desiccation or low water outgassing rates due to the desiccation of the mantle, could lead to high abundances of abiotic O_2 and O_3 in the event that the remaining atmosphere is dominated by outgassed CO_2.

The stability of CO_2 in terrestrial planet atmospheres depends on a balance between destruction by Far-UV (FUV) radiation ($\lambda \sim 121$–200 nm) from their host stars in the upper atmosphere via

$$CO_2 + h\nu \rightarrow CO + O \tag{R1}$$

and regeneration through the following catalytic cycle in the lower atmosphere:

$$H + O_2 + M \rightarrow HO_2 + M \tag{R2}$$

$$O + HO_2 \rightarrow OH + O_2 \tag{R3}$$

$$OH + CO \rightarrow CO_2 + H \tag{R4}$$

$$\overline{CO + O \rightarrow CO_2,} \tag{S1}$$

where M is a third body, and the HO_x species ($= H + OH + HO_2$) are derived from H_2O, with small contributions from H_2O_2 photolysis by Near-UV (NUV) radiation ($\lambda \sim 300$–400 nm). This process is usually faster than the spin-forbidden

regeneration reaction

$$CO + O + M \rightarrow CO_2 + M. \qquad (R5)$$
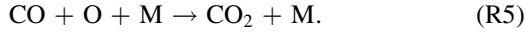
S1 is currently active on Mars and Venus (McElroy & Donahue 1972; McElroy et al. 1973; Nair et al. 1994), which explains their CO_2-dominated atmospheres despite photolysis by Solar FUV. However, M dwarfs produce much lower NUV relative to FUV due to their lower effective temperatures and intense stellar activity (West et al. 2004; Tian et al. 2014), which would reduce the efficiency of S1 while not affecting, or even increasing R1. Furthermore, if the atmospheric water content were low, as is possibly the case for terrestrial exoplanets in the M dwarf habitable zone, then S1 would be reduced even further. Previous studies that investigated CO_2 photochemistry either assumed present/young Sun-like host stars (Selsis et al. 2002; Segura et al. 2007; Zahnle et al. 2008; Hu et al. 2012) and/or ocean worlds (Domagal-Goldman et al. 2014; Tian et al. 2014). In this work, we explore the stability of CO_2 on a desiccated planet around an M dwarf and consider the potential for false positive detections of O_2 and O_3 as biosignatures.

In Section 2 we give a brief summary of the one-dimensional photochemical model we use to obtain our results, as well as describe the construction of our model atmosphere and the specific cases we considered regarding atmospheric hydrogen content. We present our results for the stability of CO_2 atmospheres in Section 3. In Section 4 we discuss the possibility for false positive detections of biosignatures, as well as consider the effects of temperature variations, clouds, hydrogen escape, and interactions between the atmosphere and the surface. We offer our conclusions in Section 5.

2. METHODS

2.1. Photochemical and Transport Model

We use the Caltech/JPL one-dimensional Photochemical model (Allen et al. 1981), as modified by Nair et al. (1994) for the Martian atmosphere. The model calculates the steady state distributions of 27 chemical species: O, O(^{1}D), O_2, O_3, N, N (^{2}D), N2, N_2O, NO, NO_2, NO_3, N_2O_5, HNO_2, HNO_3, HO_2NO_2, H, H_2, H_2O, OH, HO_2, H_2O_2, CO, CO_2, O^+, O_2^+, CO_2^+, and CO_2H^+. We refer the reader to Allen et al. (1981) for a detailed description of the general photochemical model and Table 2 of Nair et al. (1994) for the full list of reactions and associated rate constants (with minor updates) considered in our model. Table 1 gives a subset of Nair et al. (1994)'s reactions that are significant to this work.

Figure 1 shows a comparison between the solar spectrum (WMO 1985), and a spectrum of the M dwarf GJ 436 from France et al. (2013) that we use for our model, scaled such that the total flux of each star is equal to the total solar flux at 1 AU, ~1360 W m^{-2}. In addition, we show the wavelengths at which photolysis of CO_2, O_2, O_3, and H_2O_2 is most efficient. It is clear that the GJ 436 spectrum features a much higher FUV/NUV ratio than Sun-like stars, and as a result the photolysis rates of the four aforementioned species will differ between the two cases. The entire spectral range used in the model is ~100–800 nm. We assume that the spectrum of the star is fixed throughout the duration of our simulations. This ignores the effects of major flaring events or quiet periods, which we assume to be irrelevant on long time scales.

Table 1
Important Reactions Involved in CO_2 Destruction and Regeneration

	Reaction	Rate Constant
R1	$CO_2 + h\nu \rightarrow CO + O$	1.025×10^{-8}
R2	$H + O_2 + M \rightarrow HO_2 + M$	$k_0 = 7.3 \times 10^{-29}T^{-1.3}$
		$k_\infty = 2.4 \times 10^{-11}T^{0.2}$
R3	$O + HO_2 \rightarrow OH + O_2$	$3.0 \times 10^{-11}e^{200/T}$
R4	$OH + CO \rightarrow CO_2 + H$	$4.9 \times 10^{-15}T^{0.6}$
R5	$CO + O + M \rightarrow CO_2 + M$	$1.6 \times 10^{-32}e^{-2184/T}$
R6	$H_2O_2 + h\nu \rightarrow 2OH$	1.273×10^{-6}
R7	$2HO_2 \rightarrow H_2O_2 + O_2$	$3.0 \times 10^{-13}e^{460/T}$
R8	$HO_2 + O_3 \rightarrow 2O_2 + OH$	$1.0 \times 10^{-14}e^{-490/T}$
R9	$O_3 + h\nu \rightarrow O_2 + O$	2.898×10^{-6}

Notes. The rate constants are updated from those of Nair et al. (1994) using Sander et al. (2011) and references therein. Rate constants for photolysis reactions are for the top of the atmosphere. Units for photochemical, two-body, and three-body reactions are s^{-1}, cm^3 s^{-1}, and cm^6 s^{-1}, respectively. k_0 and k_∞ are the low- and high-pressure limit rate constants, respectively.
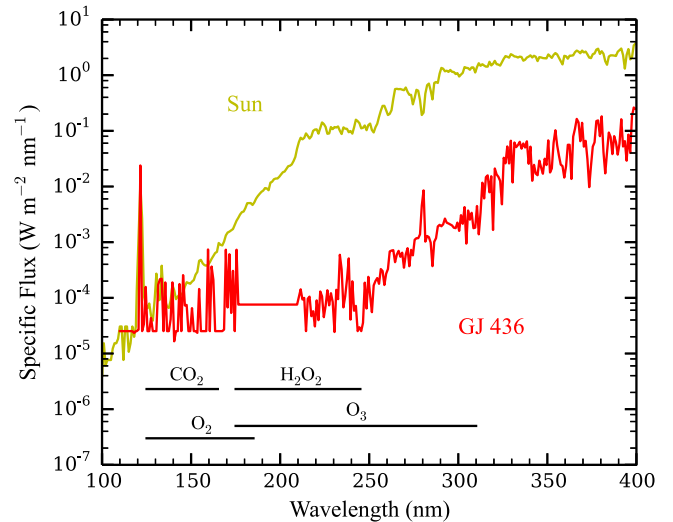

Figure 1. The spectra of the Sun (WMO 1985; yellow) and GJ 436 (France et al. 2013; red) scaled such that the total flux of each is identical to the total flux received by Earth at 1 AU (~1360 W m^{-2}). The wavelengths at which photolysis of CO_2, O_2, O_3, and H_2O_2 is most efficient are added for comparison (Tian et al. 2014).

2.2. Boundary Conditions

The choice of boundary conditions strongly affects the resulting atmospheric composition. The major processes that are typically modeled include hydrogen escape, volcanic outgassing, and surface deposition of oxidants. The rates of these processes, especially the latter two, are highly uncertain. For example, the outgassing flux of water for Earth is 10^{11}–10^{12} cm^{-2} s^{-1} (Fischer 2008), while on Venus it could be as low as 5.5×10^5–10^7 cm^{-2} s^{-1} (Walker et al. 1970; Grinspoon 1993). This is likely due to the hydrodynamic loss of water in Venus's past (Hamano et al. 2013), similar to the conditions experienced by our modeled M dwarf exoplanet. Likewise, the deposition velocity of oxidants, such as O_2 and O_3, is strongly tied to surface composition and water content. On Earth and Mars, aqueous reactions of molecular oxygen and ozone with ferrous iron, sulfides, and other reducing species act as significant sinks for oxidants, but deposition velocities on

Mars could be 10–100 times lower than on Earth due to the reduced surface humidity and differences in surface composition (Zahnle et al. 2008). Therefore, given that our modeled planet could be drier still, and that the crust and upper mantle may already be heavily oxidized, the deposition of oxidants could be severely limited.

If hydrogen escape is in the diffusion-limited regime, then the flux can be expressed as

$$\phi_{lim} = f_H(z) b_{H/H_2}^{CO_2} \left(\frac{1}{H_{CO_2}} - \frac{1}{H_{H/H_2}} \right) \qquad (1)$$

(Zahnle et al. 2008) where ϕ_{lim} is the diffusion-limited escape flux, f_H is the total mixing ratio of all hydrogen species at the homopause, $b_{H/H_2}^{CO_2}$ is the binary diffusion coefficient of hydrogen (H or H_2) escaping through CO_2, and H_x is the scale height of species x, where x = H or H_2 and CO_2. As M dwarfs emit abundant XUV ($\lambda < 121$ nm) radiation and highly charged particles that can cause hydrodynamic escape and sputtering, the rate of hydrogen loss could readily reach the diffusion-limited regime (Cohen et al. 2015), though sputtering could be reduced if a strong planetary magnetic field exists (Lammer et al. 2007). On the other hand, the abundance of hydrogen above the homopause is strongly tied to the rate of production from photolysis of water and H_2O_2, as well as chemistry in the ionosphere (Nair et al. 1994). Thus, in the limit of low atmospheric hydrogen content, the hydrogen escape flux could be much lower than the diffusion-limited flux.

Given the possibility that the outgassing, deposition, and escape fluxes may be low, we will simplify the problem and focus strictly on the effects of high UV flux, low water content, and high CO_2-content by assigning zero fluxes to all species for our upper and lower boundary conditions. We make an exception for ions, which have a zero flux upper boundary condition and a fixed concentration of 0 cm^{-3} at the lower boundary to simulate recombination with electrons at the surface (Nair et al. 1994). This is equivalent to hydrogen escape being balanced by the outgassing of water, with the outgassed oxygen atoms being lost through surface deposition of oxidants. These simplified boundary conditions, which are potentially representative of desiccated terrestrial exoplanets orbiting M dwarfs, will be evaluated in Section 4.1.

2.3. Model Atmosphere

In order to model a CO_2-dominated atmosphere we simulate Mars-like atmospheric composition with a surface atmospheric pressure of 1 bar for an Earth-sized planet with Earth's surface gravity. We keep the same (Martian) mixing ratios of atmospheric species as Nair et al. (1994). The pressure P, temperature T, and eddy diffusion coefficient K_{zz} profiles are shown in Figure 2. The model atmosphere extends from the surface to 100 km altitude with an altitude bin thickness of 1 km. The pressure profile is calculated assuming an ideal gas atmosphere in hydrostatic equilibrium.

The temperature profile is split into the troposphere, the stratosphere/mesosphere, and the thermosphere. The troposphere is assumed to be a dry adiabat with the heat capacity of CO_2 as a function of temperature taken from McBride & Gordon (1961) and Woolley (1954). The surface temperature
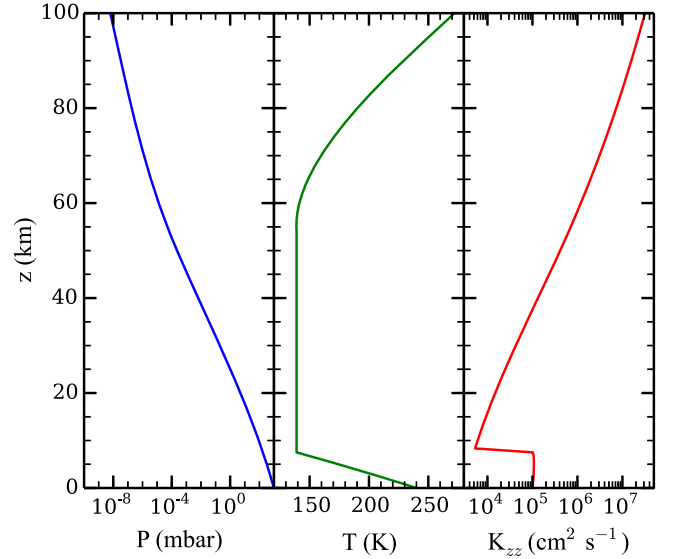

Figure 2. Model atmospheric pressure P (left), temperature T (center), and eddy diffusion coefficient K_{zz} (right) as functions of altitude z.

is assumed to be 240 K, accounting for the warming due to 1 bar of CO_2 (Kasting 1991). The temperature decreases along the adiabat with increasing altitude until it reaches the planetary skin temperature of 139 K, identical to that of Mars, by assumption (Nair et al. 1994). This places the tropopause of our atmosphere at ~7.5 km. Above the tropopause the temperature profile is assumed to be isothermal, consistent with previous works (Kasting 1990; Segura et al. 2005, 2007). The temperature increases in the thermosphere above 60 km due to inefficient collisional cooling, and the temperatures are calculated by assuming that the temperature–pressure relationship is identical in the thermospheres of both our model atmosphere and Nair et al. (1994)'s model atmosphere. This assumption is valid given the density (and thus pressure) dependence of collisional cooling (López-Puertas & Taylor 2001). As the pressure profile depends on the temperature profile, we iterate between the two until convergence.

The eddy diffusion coefficient as a function of altitude is calculated assuming free convection (Gierasch & Conrath 1985),

$$K_{zz} = \frac{H}{3} \left(\frac{L}{H} \right)^{4/3} \left(\frac{R\sigma T^4}{\mu \rho C_p} \right)^{1/3} \qquad (2)$$

where H is the scale height given by $RT/\mu g$, R is the universal gas constant, σ is the Stefan–Boltzmann constant, μ is the atmospheric molecular weight, which is assumed to be identical to that of CO_2, ρ is the atmospheric mass density, C_p is the atmospheric heat capacity, and L is the mixing length defined with respect to the convective stability of the atmosphere (Ackerman & Marley 2001),

$$L = H \quad \max(0.1, \Gamma/\Gamma_a) \qquad (3)$$

where Γ is the lapse rate and Γ_a is the adiabatic lapse rate. As with Ackerman & Marley (2001), we set a lower bound for L of $0.1H$ in the radiative regions of the atmosphere. Using Equations (1) and (2), we find a surface eddy diffusion coefficient value of 3.4×10^7 cm^2 s^{-1}, which is more than twice as high as in previous studies where a value of

$10^5 \, \mathrm{cm^2 \, s^{-1}}$ is often used (e.g., Nair et al. 1994; Segura et al. 2007). This is likely due to the equations' assumption of free convection breaking down in the presence of a solid surface. Therefore, we scale the entire profile by a constant factor such that the surface value is $10^5 \, \mathrm{cm^2 \, s^{-1}}$.

The temperature, pressure, and eddy diffusion coefficient profiles are held constant with time throughout the simulation, even when the atmospheric composition changes drastically. We will discuss how a self-consistent atmospheric model may impact our results in Section 4.3.

2.4. Atmospheric Hydrogen and Oxygen Content

The hydrodynamic loss of water leads to an atmosphere depleted in hydrogen, which is mostly bound in H_2 and H_2O in our model. To simulate such depletion we decrease the initial water content of the atmosphere such that it is undersaturated at all altitudes. Using the expression of Lindner (1988) for the temperature-dependent saturation vapor pressure of water we find the minimum value of the saturation water vapor mixing ratio of our model atmosphere to be 1.675×10^{-5} ppm at the tropopause, where the temperature is 139 K. We then vary the H_2 content to investigate the result of different degrees of hydrogen depletion in the atmosphere. We simulate six cases, with total atmospheric H mole fractions $f(H)_{tot}$ of (1) 26 ppm, (2) 2.6 ppm, (3) 0.27 ppm, (4) 0.032 ppm, (5) 0.0088 ppm, and (6) 0.0065 ppm. $f(H)_{tot}$ is defined as the number of hydrogen atoms in the atmosphere divided by the total number of atoms in the atmosphere. By comparison, the H mole fraction of Venus is 14 ppm (Miller-Ricci et al. 2009).

We assume that the excess oxygen produced from water depletion is taken up by the crust and upper mantle during the Runaway Greenhouse phase, when a magma ocean may have formed on the surface that would have acted as an extremely efficient oxygen sink (Hamano et al. 2013; Luger & Barnes 2015). The resulting atmosphere would then be low in oxygen, while the crust and upper mantle compensate by being oxidized.
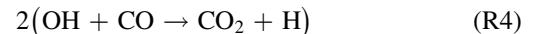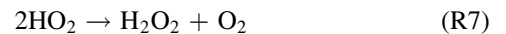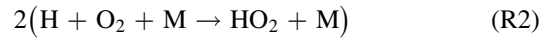
3. RESULTS

Despite the low water content of our model atmosphere, >50% of the atmospheric CO_2 present at the beginning of our simulations is retained. We find that this results from the actions of CO_2-regenerating catalytic cycles that rely on H_2O_2 and O_3 instead of H_2O, which arise due to the low M dwarf NUV flux limiting H_2O_2 and O_3 destruction by photolysis. Nonetheless, abiotic O_2 and O_3 column mixing ratios up to 20% and 1 ppm, respectively, can be produced from CO_2 photolysis, giving rise to potential false positives when using O_2 or O_3 as the signature of biological photosynthesis.

Figure 3 shows the steady state mixing ratios of several species in our model atmosphere as a function of altitude after 10 Gyr of evolution. The long-lived species, such as CO_2, CO, O_2, H_2, H_2O, and H_2O_2, tend to be well mixed below the homopause (~50 km in our model atmosphere). Above the homopause, (1) CO_2 is depleted due to photolysis, which in turn produces an excess of CO and O_2, (2) the H_2 mixing ratio increases due to molecular diffusion, and (3) H_2O and H_2O_2 are fairly well-mixed, as most of their chemistry takes place at lower altitudes. The short-lived species, as expected, are not well mixed: O_3 and HO_2 both show clear mixing ratio maxima near the homopause due to their high production rates there,

while H and OH are only abundant above the homopause due to their rapid removal below.

Figure 3 also shows a clear trend in the mixing ratios of these species as the atmospheric hydrogen content is varied. For example, as the hydrogen content drops, the hydrogen species' mixing ratios also decrease, while the O_3 mixing ratio increases. This trend is better seen in Figure 4, which shows the column-averaged mixing ratios of the same species as in Figure 3, as a function of the atmospheric hydrogen content. There is a clear trend of decreasing CO_2 with decreasing atmospheric hydrogen, eventually reaching a lower limit for cases with hydrogen mixing ratio ~1 ppm. The high abiotic O_2 and CO concentrations of our atmospheres (5%–20% and 10%–40%, respectively) are consistent with previous studies showing the propensity for planets with low atmospheric H_2O abundance to lose more CO_2 to photolysis than planets with high atmospheric H_2O abundance (e.g., Segura et al. 2007). However, we do not lose as much CO_2 as the results of Zahnle et al. (2008), which showed that an atmosphere as depleted in water as ours (~0.6 precipitable microns for our "wettest" case) should be unstable to conversion to CO if irradiated by a Sun-like star. This suggests the existence of alternate chemical pathways aside from S1 that are responsible for regenerating CO_2 in low H_2O, initially CO_2-dominated atmospheres of terrestrial planets orbiting M dwarfs. These chemical pathways must be such that (1) CO_2 still dominates even when H_2O concentrations are low, and (2) CO_2 is stopped from complete conversion to CO and O_2 even when atmospheric hydrogen is severely depleted.

Figure 5 shows the rates of several key reactions near the surface of the planet as the hydrogen content of the atmosphere is reduced from panels 1–6, which correspond to Cases 1–6, respectively, as well as the points on the column-averaged mixing ratio curves of Figure 4. As catalytic cycles require one reaction to feed into another, the reactions that make up the cycle must all have the same effective reaction rate, determined by the rate-limiting step. Thus, for Case 1, R2, R4, R6, and R7 form a catalytic cycle below 20 km:

$$2(H + O_2 + M \rightarrow HO_2 + M) \quad \text{(R2)}$$

$$2HO_2 \rightarrow H_2O_2 + O_2 \quad \text{(R7)}$$

$$H_2O_2 + h\nu \rightarrow 2OH \quad \text{(R6)}$$

$$2(OH + CO \rightarrow CO_2 + H) \quad \text{(R4)}$$

$$\overline{2CO + O_2 \rightarrow 2CO_2.} \quad \text{(S2)}$$

This cycle depends on relatively high concentrations of H_2O_2, which replaces water as the major reservoir/source of HO_x species. The lower panel of Figure 4 shows that the equilibrium H_2O_2 mixing ratio for the highest H_2 case is ~0.2 ppm, which is ~20 times higher than the modeled Martian H_2O_2 mixing ratio from Nair et al. (1994). This buildup of H_2O_2 is due to its low photolysis rate around M dwarfs. S2 has been considered as a CO_2 regeneration pathway for a wet Mars (Parkinson & Hunten 1972; Yung & DeMore 1999), which relies on high H_2O_2 abundances arising from high H_2O abundances.

As the atmospheric hydrogen content is decreased from Cases 1–3 in Figure 5, the mixing ratios of H_2O_2 and HO_2 decrease (see Figure 4), resulting in a drop in the rates of R6 and R7. Consequently, S2 becomes less efficient at regenerating CO_2. This leads to the decrease in CO_2 and the increase in CO and O_2 shown in Figure 4, which in turn results in the
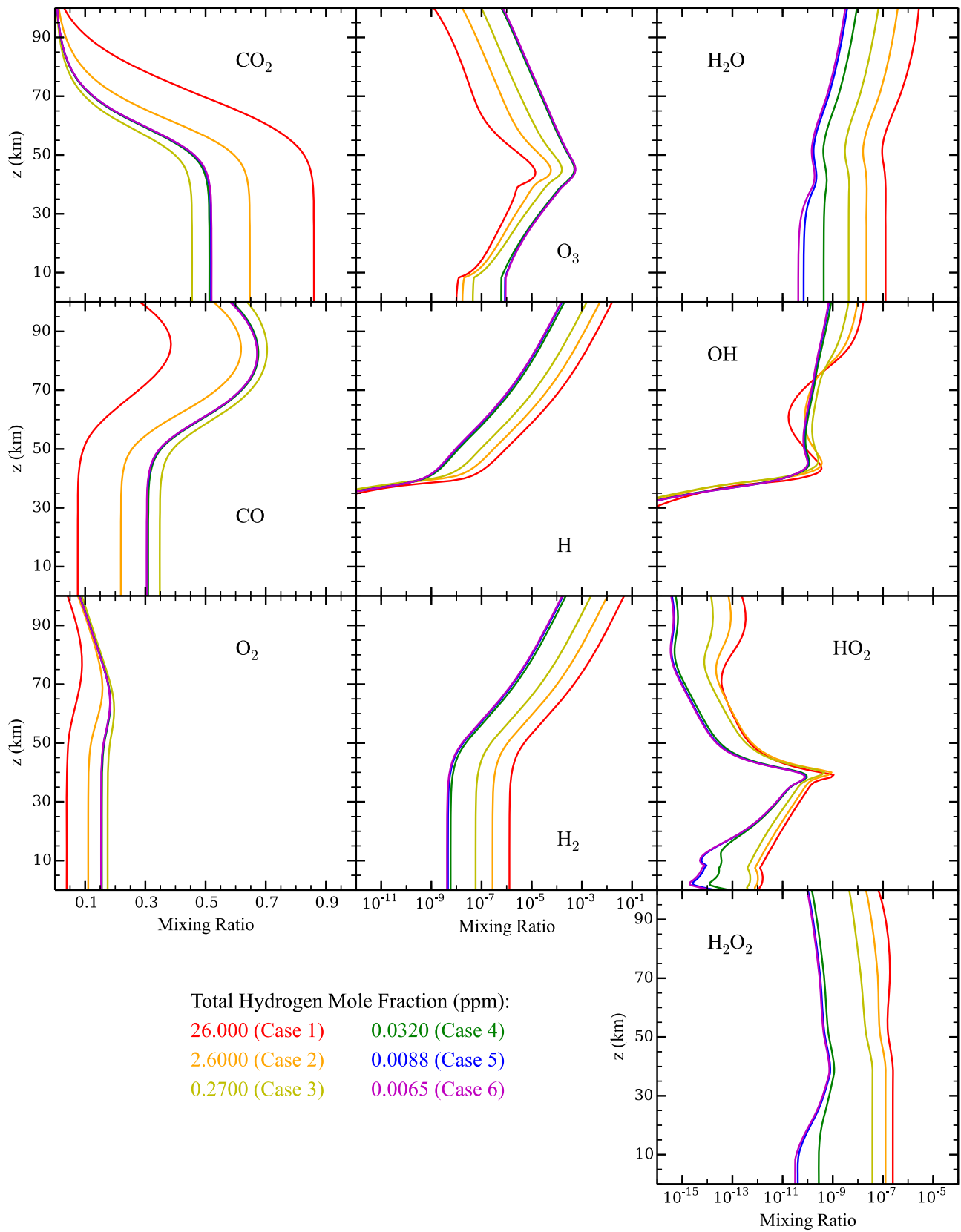
Figure 3. Mixing ratio profiles of CO_2, CO, O_2, O_3, H, H_2, H_2O, OH, HO_2, and H_2O_2 for Cases 1 (red), 2 (orange), 3 (yellow), 4 (green), 5 (blue), and 6 (magenta). Note the different x-axis values for the three different columns. For many of the species, the curves for cases 4, 5, and 6 overlap each other.
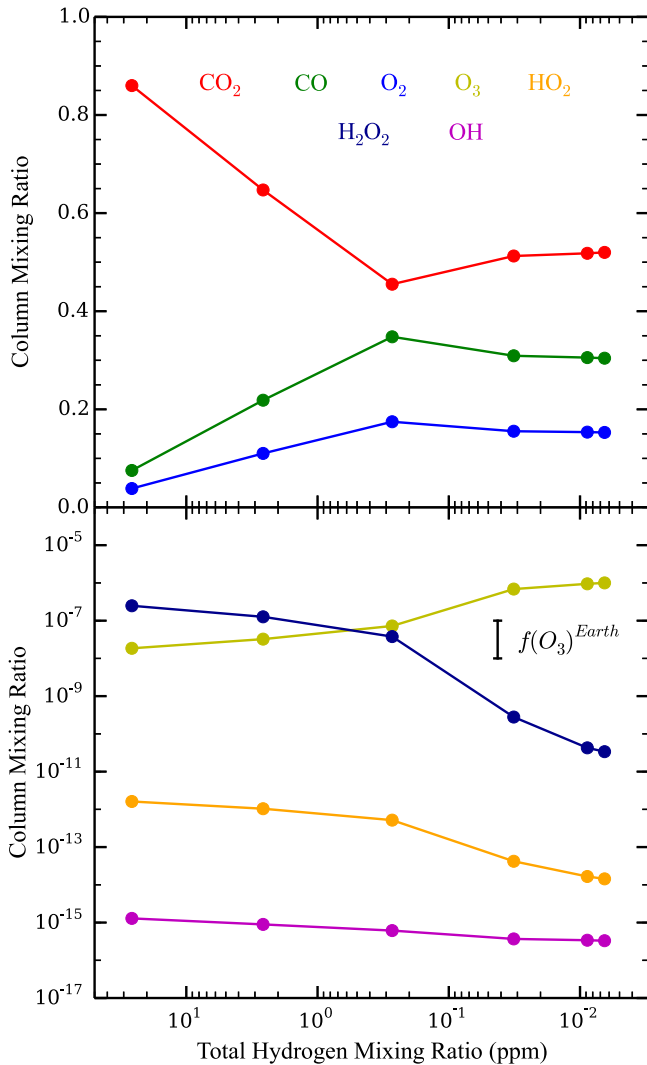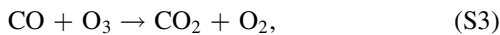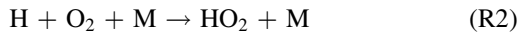
Figure 4. Column-integrated mixing ratios of (top) CO_2 (red), CO (green), O_2 (blue), (bottom) O_3 (yellow), HO_2 (orange), H_2O_2 (dark blue), and OH (magenta) as functions of the total atmospheric hydrogen mole fraction for Cases 1 through 6. This mole fraction is calculated by dividing the number of hydrogen atoms in the atmosphere by the total number of atoms in the atmosphere. The points indicate the results of the actual cases, which are connected by lines. In the bottom panel we show the range in Earth's O_3 mixing ratio $f(O_3)^{Earth}$ (Yung & DeMore 1999). Note the different y-axis scales of the top and bottom panels.

increase in O_3. The rise of ozone increases the rate of R8 and its own photolysis reaction R9, which produces an abundance of free oxygen atoms that go into increasing the rate of R5. Eventually, R8 replaces R6 and R7 in S2, forming

$$H + O_2 + M \rightarrow HO_2 + M \qquad (R2)$$

$$O_3 + HO_2 \rightarrow OH + 2O_2 \qquad (R8)$$

$$OH + CO \rightarrow CO_2 + H \qquad (R4)$$

$$CO + O_3 \rightarrow CO_2 + O_2, \qquad (S3)$$

which, together with R5, dominates the CO_2 regeneration process below 15 km. Case 3 shows the switch from S2 to S3 and R5, where neither process is particularly efficient; this causes the minimum in the CO_2 mixing ratio curve in Figure 4. The increase in O_3 concentrations goes on to increase the rates

of S3 and R5 in Cases 4–6, which in turn explains the upswing in the CO_2 mixing ratio seen in Figure 4 for the cases with atmospheric hydrogen content <0.1 ppm. The importance of O_3 in S3 and R5 creates a negative feedback, where excess CO_2 photolysis produces excess O_2 and O_3, which then increases the intensity of CO_2 regeneration via S3 and R5. This stops further decreases in the CO_2 mixing ratio with decreasing atmospheric hydrogen content. S3 has been recognized as a major catalytic cycle for the loss of O_3 on M dwarf exoplanets by Grenfell et al. (2013), but they considered an atmosphere similar to that of modern Earth instead of a CO_2-dominated atmosphere like that of our model.

Further evidence of the importance of O_3 to CO_2 regeneration in these low atmospheric hydrogen/water cases is given in Figure 6, which shows molecular fluxes from Case 1 (top) and Case 6 (bottom) near the planet surface for O_2, O_3, CO, and CO_2. The fluxes of Case 1 show a balance between downwelling CO and upwelling CO_2, consistent with the conversion from CO to CO_2 occurring near the surface by S2. The fluxes of Case 6 are similar, but, in addition, O_2 and O_3 also have a correspondence, with conversion of O_3 to O_2 occurring near the surface in keeping with S3.

For the cases where the atmospheric hydrogen mixing ratio is <0.05 ppm, as in Cases 5 and 6 of Figure 5, R5 dominates and S3 is reduced, due to low HO_2 and OH concentrations. Further decreases in atmospheric hydrogen content are inconsequential since R5 does not depend on any hydrogen species.

The importance of H_2O_2 and O_3 photolysis for S2, S3, and R5 means our results would differ significantly for similar planets around Sun-like stars. Aside from the lack of a prolonged high luminosity pre-main sequence phase, Sun-like stars also emit more strongly in the NUV, resulting in higher rates of H_2O_2 and O_3 photolysis (see Figure 1). Therefore, only a small amount of H_2O_2 and O_3 is necessary to produce the photolysis products needed to regenerate CO_2. An alternate simulation of Case 6 that uses a Solar spectrum rather than an M dwarf spectrum yields ∼2% O_2 and 4% CO, consistent with the results of previous works that used solar spectra (e.g., Hu et al. 2012). Though these values are lower than our nominal results, they are still ∼100 times higher than that of a non-desiccated planet orbiting a Sun-like star, such as Earth during the Proterozoic eon (Planavsky et al. 2014). This suggests that false positive detections of biosignatures are possible even for desiccated planets around Sun-like stars. These results are also similar to those of Nair et al. (1994) when they only used R5 for CO_2 regeneration, though there is more CO_2 remaining at equilibrium in our case due to the higher atmospheric density, which increases the rate of R5.

4. DISCUSSION

4.1. Surface Fluxes and Atmospheric Escape

We have assumed zero-flux boundary conditions for all neutral species in our model atmosphere in order to simplify the problem and focus on the effects of high UV flux, low water content, and high CO_2-content. This is equivalent to assuming that all fluxes are nonzero, but are in balance with each other. In this section we evaluate this assumption by introducing explicit, balanced fluxes into our model with the goal of determining what surface and escape fluxes are necessary to
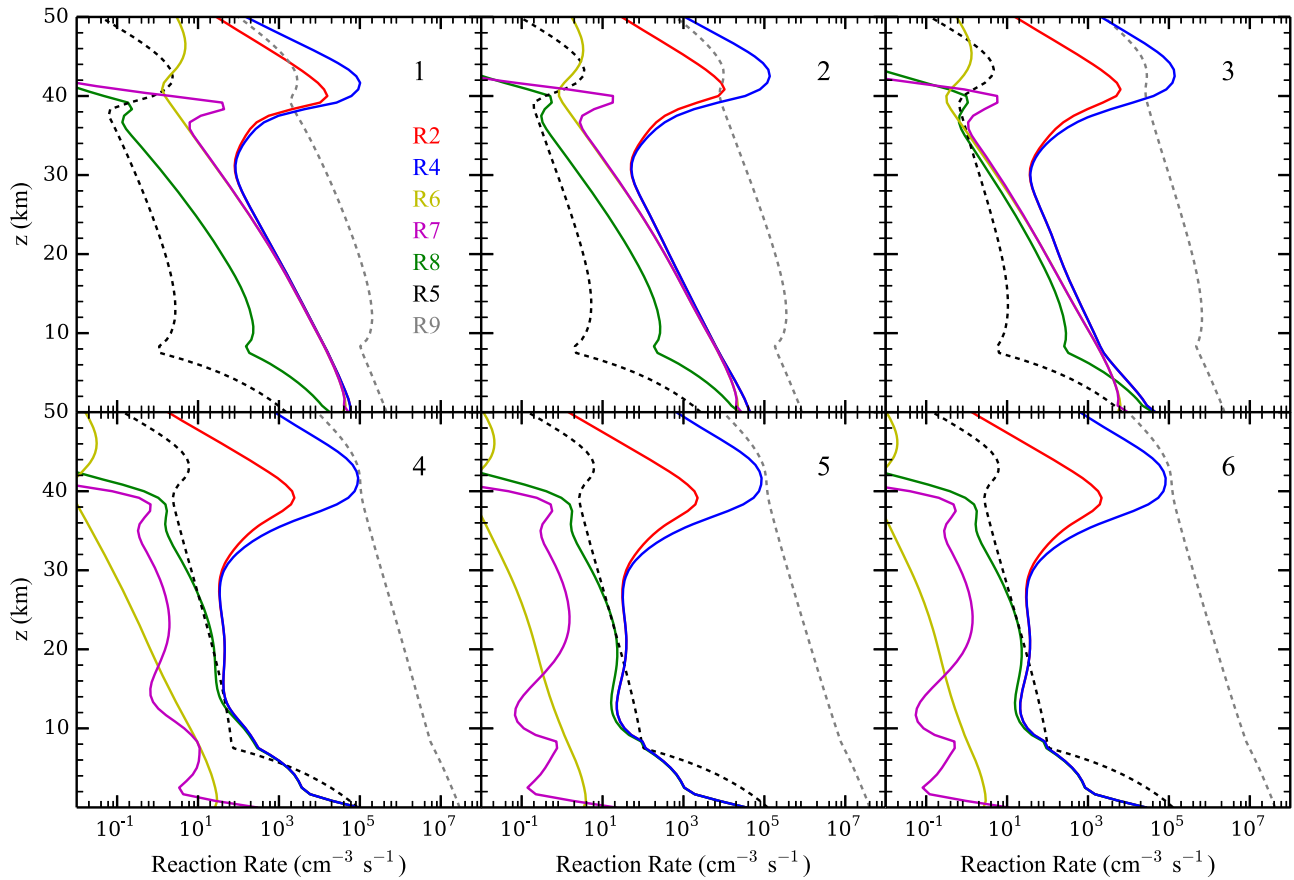
Figure 5. Reaction rates of R2: $H + O_2 + M \rightarrow HO_2 + M$ (red), R4: $OH + CO \rightarrow CO_2 + H$ (blue), R5: $CO + O + M \rightarrow CO_2 + M$ (black, dotted line), R6: $H_2O_2 + h\nu \rightarrow 2OH$ (yellow), R7: $2HO_2 \rightarrow H_2O_2 + O_2$ (magenta), R8: $HO_2 + O_3 \rightarrow 2O_2 + OH$ (green), and R9: $O_3 + h\nu \rightarrow O_2 + O$ (gray, dotted line) as functions of altitude in the lower atmosphere for (1) Case 1, $f(H)_{tot} \sim 26$ ppm; (2) Case 2, $f(H)_{tot} \sim 2.6$ ppm; (3) Case 3, $f(H)_{tot} \sim 0.27$ ppm; (4) Case 4, $f(H)_{tot} \sim 0.032$ ppm; (5) Case 5, $f(H)_{tot} \sim 0.0088$ ppm; and (6) Case 6, $f(H)_{tot} \sim 0.0065$ ppm.

reproduce our zero-flux results, and thus what planets may possess these atmospheric compositions. The fluxes modeled are the outgassing of H_2O, the escape of H and H_2 into space, and the surface deposition of O_3. O_2 deposition is assumed to be zero due to its relatively low reactivity and solubility in water compared to O_3 (Sonntag & von Gunten 2012), though its high abundance in the drier cases may increase its significance (see below). Comparisons between the zero-flux and explicit flux models are done using our wettest and driest cases, Cases 1 and 6, respectively. All other run parameters of the models are identical to the corresponding zero-flux cases.

Figure 7 shows the comparison between the mixing ratios derived from the explicit flux model (dashed curves) and that derived from our nominal model (solid curves), for Cases 1 (red) and 6 (blue). There is satisfactory agreement between the two models for almost all of the species, including those vital to the catalytic cycles outlined in Section 3. The major difference between the two models is the reservoir of atmosphere hydrogen. For the zero-flux case, the reservoirs are H_2 and H_2O_2, while in the explicit flux model the hydrogen reservoir is water. This is understandable since water is being actively replenished by outgassing, and the production of H and H_2 is dependent on the H_2O abundance. This leads to a slight decrease in H and H_2 mixing ratios, which further leads to the minor differences in the abundances of the other species.

Table 2 shows the escape velocities/fluxes, outgassing fluxes, and surface deposition velocities/fluxes for Cases 1 and 6 of the explicit flux model. The hydrogen escape

velocities, which were derived using Case 1 and then applied to Case 6, are consistent with the diffusion-limited escape velocity of hydrogen at Earth's homopause (Hunten 1973). We found that greater escape velocities led to the depletion of hydrogen in the upper atmosphere with respect to the zero-flux results, while lower velocities led to excesses of H and H_2 without any changes in the shapes of their profiles. The hydrogen escape flux for Case 1 is consistent with that of Venus (Grinspoon 1993), which is unsurprising given their similar atmospheric hydrogen mole fractions (Miller-Ricci et al. 2009), while Case 6 has much lower escape fluxes, in accordance with its lower atmospheric hydrogen content. The same pattern holds for water outgassing: The flux for Case 1 is similar to that of Venus (5.5×10^5–10^7 cm^{-2} s^{-1}), while that of Case 6 is an order of magnitude lower than the given lower limit of the Venus water outgassing flux (Walker et al. 1970). By analogy this could mean that volcanism rates, and thus heat fluxes, are relatively high, but the water content of the lava is much lower. This is consistent with a desiccated upper mantle that lost its hydrogen during the early runaway greenhouse-induced magma ocean phase (Hamano et al. 2013; Luger & Barnes 2015).

The deposition of oxidants is crucial in determining the oxidative state of the atmosphere. For example, in the work of Zahnle et al. (2008), where H_2O_2 and O_3 are lost to aqueous reactions with ferrous iron and sulfides, the atmosphere tends to be converted entirely to CO. As O_3 and H_2O_2 are crucial to the catalytic cycles we have outlined, it is not surprising that losing
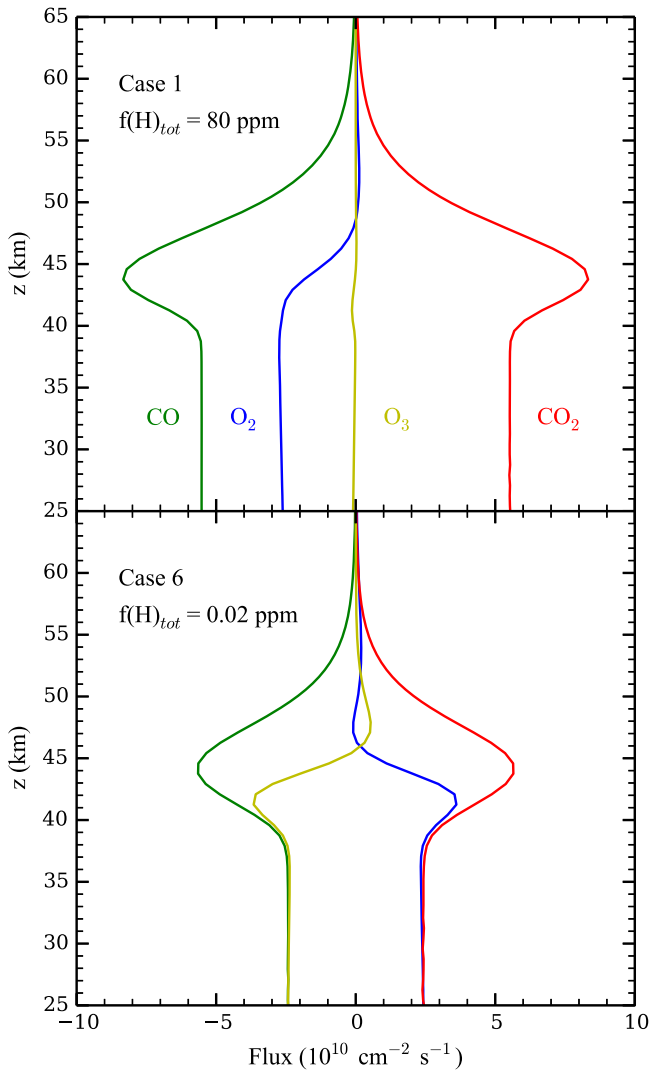
Figure 6. Vertical fluxes of O_2 (blue), O_3 (yellow), CO_2 (red), and CO (green) in the lower atmosphere for Cases 1 (top) and 6 (bottom). Upward fluxes are positive while downward fluxes are negative.

them to the surface would result in high CO concentrations, as the efficiency of CO_2 regeneration would be vastly decreased. Zahnle et al. (2008) used an O_3 deposition velocity of $0.02 \, cm \, s^{-1}$ for the surface of Mars, which is 3 and 8 orders of magnitude greater than that of our explicit flux results for Cases 1 and 6, respectively. Such low deposition velocities may be consistent with a surface much drier than that of Mars. Zahnle et al. (2008) used a surface relative humidity of water of 17% for their Mars model, which is 320 times higher than the relative humidity for our Case 1 results, and 8.5×10^5 times higher than that of our Case 6 results. Therefore, it is plausible that our deposition velocities are low due to the lack of an aqueous medium within which oxidation can proceed quickly. However, the exact relationship between O_3 deposition velocity and relative humidity is unknown, especially for very low water abundances. Alternatively, the planetary surface may be low in ferrous iron and sulfides due to the oxidation resulting from burial of hundreds of bars of oxygen during the aforementioned magma ocean phase.

Similar arguments can be made for O_2 deposition. Zahnle et al. (2008) attributed the surface flux of O_2 on Mars to UV photostimulated oxidation of magnetite in the presence of trace

amounts of water. However, this may be insignificant in our case due to the low UV flux at our model planet's surface, as a result of our thicker atmosphere. Therefore, any O_2 flux at the surface is likely due to aqueous reactions with reducing species, as with O_3. An alternative simulation of the explicit flux cases using O_2 deposition instead of O_3 deposition yielded velocities of $3.7 \times 10^{-12} \, cm \, s^{-1}$ and $3 \times 10^{-15} \, cm \, s^{-1}$ for Cases 1 and 6, which are 5 and 8 orders of magnitude lower, respectively, than that assumed by Zahnle et al. (2008) for UV photostimulation ($4 \times 10^{-7} \, cm \, s^{-1}$). Despite the different depositional mechanisms, these differences are similar in magnitude to that of our O_3 deposition results. Therefore, as both UV photostimulation and aqueous chemistry require some water, the reduced relative humidity at the surface of our desiccated planet may inhibit O_2 deposition by either mechanism just as it does O_3 deposition.

These calculations show that terrestrial planets that have experienced severe loss of water and oxidization of the crust and upper mantle, such as planets orbiting in the habitable zones of M dwarfs, can potentially possess an atmosphere similar to our zero-flux results provided that CO_2 is abundant in their atmospheres. Consequently, biosignature false positives may be prevalent for planets orbiting in the habitable zone of M dwarfs, and should be taken into consideration in future studies and observation campaigns, as we discuss below.

4.2. Biosignature False Positives

Our results show that O_2 mixing ratios of $\sim$20% and O_3 mixing ratios >1 ppm are achievable on H_2O-depleted M dwarf terrestrial exoplanets due to photochemistry. These values are similar to that of modern Earth (Yung & DeMore 1999), where the abundant O_2 and O_3 are produced by biological photosynthesis. In this section we calculate their spectral signatures and consider their impact as potential false positive biosignatures.

Figure 8 shows the thermal emission spectrum of our model atmosphere for Cases 1 (red), 3 (orange), and 6 (green), as generated by the Spectral Mapping Atmospheric Radiative Model (SMART; Meadows & Crisp 1996). We also plot the spectrum of Earth (black) generated by the extensively validated Virtual Planetary Laboratory (VPL) 3D spectral Earth model (Robinson et al. 2010, 2011, 2014), divided by two for comparison. We see immediately that not only are our three cases difficult to separate, but all three cases are very different from Earth's atmosphere as seen in the mid-IR. This is mostly due to the completely different temperature profile assumed and the lack of water vapor, which absorbs at 6.3 and beyond 18 μm, though there is a slight decrease in flux at 6.3 μm for our wettest case (Case 1). Our model atmosphere also lacks methane, which absorbs at 7.7 μm. All spectra feature a deep 15 μm CO_2 band, though it is deeper for our model atmosphere due to the cooler stratosphere. Finally, there is weak O_3 absorption at 9.7 μm that gets progressively stronger as our model atmosphere becomes drier, but it never approaches the strength of O_3 absorption in Earth's atmosphere. The weakness of this absorption is caused by the emission occurring near the surface, such that the brightness temperature of the O_3 absorption is similar to the surface temperature, which sets the continuum on either side of the absorption feature. Thus, from the thermal emission there is a clear distinction between actual Earth-like planets and those
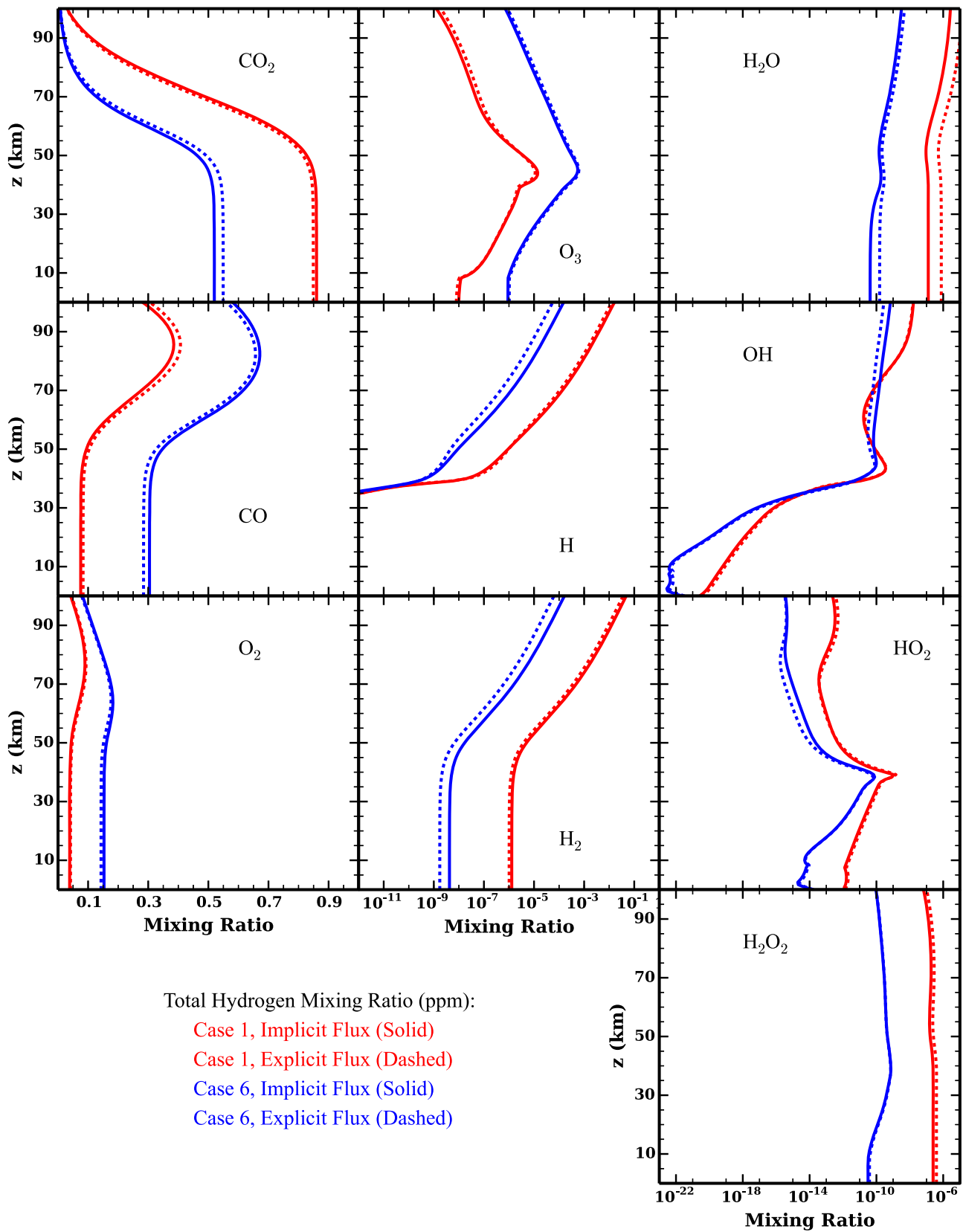
Figure 7. Mixing ratio profiles of CO_2, CO, O_2, O_3, H, H_2, H_2O, OH, HO_2, and H_2O_2 for Case 1 of the nominal, zero-flux model (red, solid), Case 1 of the explicit flux model (red, dashed), Case 6 of the nominal model (blue, solid), and Case 6 of the explicit flux model (blue, dashed). Note the different *x*-axis values for the three different columns.

Table 2
Boundary Conditions for the Explicit Flux Model that Reproduced the Corresponding Cases for the Zero-flux Model

	Case 1	Case 6
H escape velocity/flux	$5.5/1.2 \times 10^7$	$5.5/6 \times 10^4$
H_2 escape velocity/flux	$0.3/2 \times 10^6$	$0.3/3 \times 10^3$
H_2O outgassing flux	8×10^6	3.3×10^4
O_3 deposition velocity/flux	$10^{-5}/2.7 \times 10^6$	$3 \times 10^{-10}/1.1 \times 10^4$

Note. All velocities are given in units of cm s^{-1} and all fluxes are given in units of cm^{-2} s^{-1}.
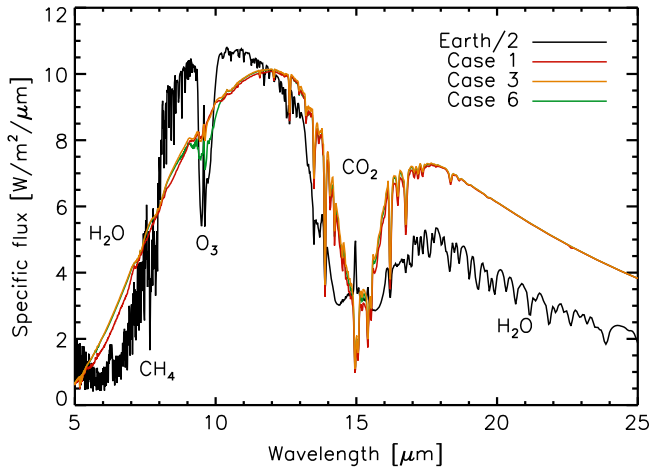

Figure 8. Thermal emission spectra of our model atmosphere for cases 1 (red), 3 (orange), and 6 (green) in the mid-IR compared to that of Earth (black; Robinson et al. 2011), divided by 2 for comparison.
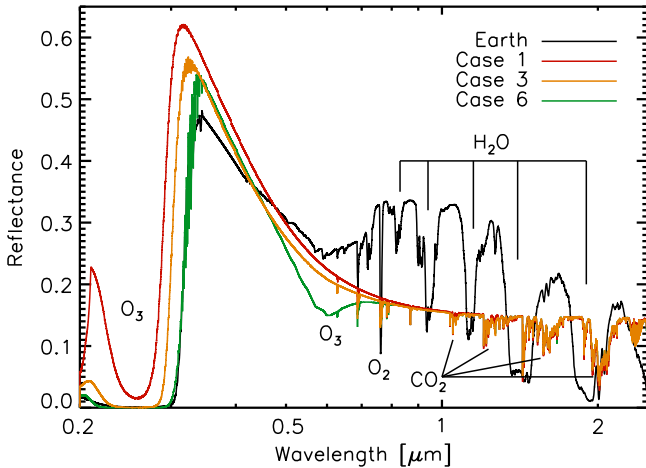

Figure 9. Normalized reflectance of our model atmosphere for cases 1 (red), 3 (orange), and 6 (green) from the near-UV to the near-IR compared to that of Earth (black; Robinson et al. 2011). A gray surface albedo of 0.15 is assumed for our model planet.

with abundant atmospheric O_2 and O_3 caused by low water content and photolysis.

Figure 9 shows the normalized reflectance of the same cases as in Figure 8 compared to the reflectance of Earth, again generated by SMART and the VPL Earth model, respectively. A gray surface albedo of 0.15 is assumed for our model planet. We see that the O_3 in our model atmosphere can be detected via deep O_3 absorption in the NUV similar in strength to O_3 absorption in Earth's atmosphere, and our driest case (Case 6)

even features a deeper Chappuis band ($\sim 0.6\,\mu m$) than Earth. However, whereas all of our cases exhibit a smooth fall-off in reflectance past $0.7\,\mu m$, punctuated by CO_2 absorption, Earth's reflectance in this region is dominated by water absorption, and thus water again acts as the discriminating species between Earth and our model planet.

From these comparisons it is clear that the condition necessary to produce abundant O_2 and O_3 in CO_2-dominated atmospheres—low water content—leads to a clear distinction in planetary spectra from those of Earth-like planets via the disappearance of strong water vapor absorption bands. Thus, biologically active, Earth-like planets can be distinguished from the planetary environments presented here using the $0.95\,\mu m$ water vapor band, the numerous water bands throughout the nearinfrared, or, in the thermal infrared, the $6.3\,\mu m$ water band, which are all observable by *JWST* (Beichman et al. 2014). However, caution must be exercised, as high-altitude cloud cover could potentially mask spectral signatures of water vapor.

4.3. Atmospheric Evolution

In our calculations we fix the pressure, temperature, and eddy diffusion coefficient profiles. As we have shown, considerable atmospheric evolution occurs over the 10 Gyr duration of each simulation, including the formation of a significant O_3 layer comparable to that of Earth and the conversion of $\sim 40\%$ of the atmospheric CO_2 into CO and O_2. Furthermore, the liberation of CO and O from CO_2 increases the total number of molecules in the atmosphere, but this should be balanced by the decrease of the molecular weight of the atmosphere from ~ 44 to ~ 37 g mol^{-1}, thereby increasing the scale height such that local number densities should remain constant. The O_3 layer in the stratosphere should raise the temperature such that a temperature inversion results due to heating by photolysis, much like in Earth's stratosphere (Park & London 1974). The decrease in CO_2 should result in warming of the stratosphere and mesosphere due to lower rates of radiative cooling (Roble & Dickinson 1989; Brasseur & Solomon 2005), as well as a cooling of the troposphere due to decreased greenhouse effects. Finally, the increase in O_2 should result in heating by photolysis in the mesosphere and thermosphere (Park & London 1974). In all, the temperature profile should increase above the tropopause and evolve in shape toward that of Earth, while below the tropopause the temperature will likely decrease.

The reaction rates will change in response to these temperature variations, as most of the reaction rate constants are exponential functions of inverse temperature (Table 1). Of the chemical reactions considered here, R2 (low pressure limit), R3, and R7 have rate constants that are inversely proportional to temperature, while R2 (high pressure limit), R4, R5, and R8 have rate constants that are directly proportional to temperature. Of the photolysis reactions, R1 decreases for decreasing temperatures (Schmidt et al. 2013) and R6 varies negligibly with temperature (Nicovich & Wine 1988). Photolysis of O_2 and O_3 (R9) decrease slightly with decreasing temperatures (Hudson et al. 1966; Lean & Blake 1981).

The combination of the temperature changes and the response of the reaction rates seem to suggest that (1) CO_2 destruction will increase as temperature increases in the stratosphere, (2) CO_2 regeneration via S2 and S3 will decrease

due to decreasing temperatures in the troposphere, and (3) CO_2 regeneration via R5 will also decrease, again due to the cooler troposphere. In other words, the atmosphere may lose much more CO_2 if the temperature evolution were taken into account. Quantitatively verifying these hypotheses require running coupled photochemistry and radiative transfer models, which is beyond the scope of this study.

4.4. Condensation

For many of our cases, H_2O is supersaturated in the stratosphere/mesosphere by the end of the 10 Gyr model run due to equilibration among the different hydrogen species. The formation of ice clouds would affect the UV radiation environment in the lower atmosphere, but whether the UV is enhanced or attenuated depends on location above or below the clouds, the solar zenith angle, cloud particle properties and distribution, and cloud optical depth. Typical variations in UV intensity on Earth's surface due to clouds are on the order of 25% in either direction while enhancement tends to occur above the clouds (Bais et al. 2006). Given the degree of supersaturation in our wetter runs, however, attenuation is more likely than enhancement below the clouds. This would decrease the H_2O_2 and O_3 photolysis rates and cause an increase in the number densities of these species, which in turn would decrease the efficiency of S2 and R5 while increasing the efficiency of S3. The magnitude to which these pathways change will depend on how much UV is attenuated as a function of wavelength, as well as the variability time scale of the clouds—if this time scale is sufficiently short, it may be irrelevant for the long time scales considered here.

The existence of water ice clouds may also result in heterogeneous chemistry that impacts the stability of CO_2 (Atreya & Blamont 1990). For example, observations of high O_3 mixing ratios over the northern polar region of Mars during northern spring is likely due to the uptake of HO_x radicals by cloud particles (Lefèvre et al. 2008). If similar processes occurred in our model atmosphere, then the decrease in HO_x species would reduce the efficiency of S2 and S3, while the buildup in O_3 would increase the efficiency of S3 and R5. As S2 is responsible for the highest rate of CO_2 regeneration, inclusion of heterogeneous chemistry will likely result in reduced amounts of CO_2, even when the atmospheric hydrogen content is relatively high. This is consistent with simulations of the Martian atmosphere that included heterogeneous chemistry (Atreya & Gu 1994; Lefèvre et al. 2008). The magnitude of these effects will depend on the reactive surface area of the cloud particles and the amount of condensable water vapor in the atmosphere.

In drier cases, the lack of significant cloud formation and rainout may produce a substantial silicate dust layer, as in the near-surface atmosphere of Mars (Hamilton et al. 2005). These particles may also participate in heterogeneous chemistry and UV attenuation (Atreya & Gu 1994), though the magnitude of the effect is likely less than that of water ice particles (Nair et al. 1994).

5. SUMMARY AND CONCLUSIONS

We have investigated the stability of H_2O—depleted, CO_2—dominated atmospheres of terrestrial exoplanets orbiting near the outer edge of the habitable zones of M dwarfs. These atmospheres may be common due to the desiccation and

oxidation of the outer layers of these planets during the host stars' pre-main sequence, when it is much more luminous than later in its evolution. We found that these atmospheres are stabilized against photolytic conversion to CO by a series of catalytic cycles and reactions. On Mars, CO_2 is maintained through the generation of free hydrogen via water photolysis leading to the oxidation of CO by HO_x species. By comparison, for a planet orbiting an M dwarf with severe water depletion, H_2O_2 photolysis dominates as the main driver of CO_2 regeneration due to the lower NUV fluxes of M dwarfs leading to a buildup of H_2O_2. This cycle is capable of maintaining 80%–90% of the original CO_2 content of the atmosphere. However, for atmospheric hydrogen content <1 ppm, H_2O_2 and HO_2 concentrations decrease and the H_2O_2 cycle (S2) breaks down, resulting in decreasing CO_2 and increasing O_2 and CO. The rise in O_2 leads to higher O_3 mixing ratios, which can now participate in the CO_2 regeneration process. Due to the low HO_2 concentrations, the O_3 cycle (S3) can only maintain half of the CO_2 in the original atmosphere. If the atmospheric hydrogen content is <0.1 ppm, any reactions involving H-species such as H or HO_2 become irrelevant, and the spin-forbidden recombination reaction R5 dominates. This reaction is actually more effective than S3, as O_3 (the source of O) increases in abundance as H decreases, and thus only 40% of the atmospheric CO_2 is converted to CO and O_2. These values may be subject to change given different atmospheric temperatures or surface pressures, but these catalytic cycles and reactions are likely general due to their self-limiting nature, i.e., if one catalytic cycle is inefficient, then another will take over.

Our model produces abundances of abiotic O_2 and O_3 comparable to that produced by photosynthetic organisms on modern Earth. This is due to our assumption of a low-H_2O atmosphere and dry surface, which decreases the CO_2 regeneration rate and the surface deposition rate of oxidizing species. These conditions may be applicable to terrestrial exoplanets in the habitable zones of M dwarfs (Luger & Barnes 2015). The high mixing ratios of O_2 and O_3 can potentially pose as false positives in the search for biosignatures, but a simultaneous search for water vapor could potentially differentiate between an actual Earth-like planet with biologically mediated atmospheric disequilibrium from a water-depleted planet with atmospheric disequilibrium caused by photochemistry. However, cloud cover can dilute this effect by decreasing the strength of water features. Meanwhile, if surface deposition were significant, then the catalytic cycles would break down due to loss of O_3 to the surface resulting in low O_2 and O_3 abundances. This would lead to much greater losses of CO_2 and ultimately the formation of a CO atmosphere.

The sensitivity of these results to temperature changes and clouds is highly complex and nonlinear, owing to the unknowns in UV-cloud radiative transfer, heterogeneous chemistry, and the feedback between temperature and reaction rates. A coupled photochemical and radiative transfer model may be necessary to fully elucidate the evolution of these exotic atmospheres.

REFERENCES

Ackerman, A. S., & Marley, M. S. 2001, ApJ, 556, 872
Allen, M., Yung, Y. L., & Waters, J. W. 1981, JGR, 86, 3617
Atreya, S. K., & Blamont, J. E. 1990, GeoRL, 17, 287
Atreya, S. K., & Gu, Z. G. 1994, JGR, 99, 13133
Bais, A. F., Lubin, D., Arola, A., et al. 2006, Scientific Assessment of Ozone Depletion (Ch.7; Geneva: WMO)
Beichman, C., Benneke, B., Knutson, H. A., et al. 2014, PASP, 126, 1134
Brasseur, G. P., & Solomon, S. 2005, Aeronomy of the Middle Atmosphere (3rd ed.; Dordrecht: Springer)
Cohen, O., Ma, Y., Drake, J. J., et al. 2015, ApJ, 806, 41
Domagal-Goldman, S. D., Segura, A., Claire, M. W., et al. 2014, ApJ, 792, 90
Fischer, T. P. 2008, GeocJ, 42, 21
France, K., Froning, C. S., Linsky, J. L., et al. 2013, ApJ, 763, 149
Gierasch, P. J., & Conrath, B. J. 1985, in Recent Advances in Planetary Meteorology, ed. G. E. Hunt (New York: Cambridge Univ. Press), 121
Grenfell, J. L., Gebauer, S., Godolt, M., et al. 2013, AsBio, 13, 415
Grinspoon, D. H. 1993, Natur, 363, 428
Hamano, K., Abe, Y., & Genda, H. 2013, Natur, 497, 607
Hamilton, V. E., McSween, H. Y., Jr., & Hapke, B. 2005, JGR, 110, E12006
Hayashi, C. 1961, PASJ, 13, 450
Hu, R., Seager, S., & Bains, W. 2012, ApJ, 761, 166
Hudson, R. D., Carter, V. L., & Stein, J. A. 1966, JGR, 71, 2295
Hunten, D. M. 1973, JAtS, 30, 1481
Kasting, J. F. 1990, OLEB, 20, 199
Kasting, J. F. 1991, Icar, 94, 1
Lammer, H., Lichtenegger, H. I. M., Kulikov, Y. N., et al. 2007, AsBio, 7, 185
Lean, J. L., & Blake, A. J. 1981, JGR, 86, 211
Lefèvre, F., Bertaux, J.-L., Clancy, R. T., et al. 2008, Natur, 454, 971
Lindner, B. L. 1988, P&SS, 36, 125
López-Puertas, M., & Taylor, F. W. 2001, Non-LTE Radiative Transfer in the Atmosphere (Singapore: World Scientific)
Luger, R., & Barnes, R. 2015, AsBio, 15, 119
Meadows, V. S., & Crisp, D. 1996, JGR, 101, 4595
McBride, B. J., & Gordon, S. 1961, JChPh, 35, 2198
McElroy, M. B., & Donahue, T. M. 1972, Sci, 177, 986
McElroy, M. B., Sze, N. D., & Yung, Y. L. 1973, JAtS, 30, 1467
Miller-Ricci, E., Seager, S., & Sasselov, D. 2009, ApJ, 690, 1056
Nair, H., Allen, M., Anbar, A. D., et al. 1994, Icar, 111, 124
Nicovich, J. M., & Wine, P. H. 1988, JGR, 93, 2417
Park, J. H., & London, J. 1974, JAtS, 31, 1898
Parkinson, T. D., & Hunten, D. M. 1972, JAtS, 29, 1380
Planavsky, N. J., Reinhard, C. T., Wang, X., et al. 2014, Sci, 31, 635
Quintana, E. V., Barclay, T., Raymond, S. N., et al. 2014, Sci, 344, 277
Robinson, T. D., Meadows, V. S., & Crisp, D. 2010, ApJL, 721, L67
Robinson, T. D., Meadows, V. S., Crisp, D., et al. 2011, AsBio, 11, 393
Robinson, T. D., Ennico, K., Meadows, V. S., et al. 2014, ApJ, 787, 171
Roble, R. G., & Dickinson, R. E. 1989, GeoRL, 16, 1441
Sander, S. P., Abbatt, J., Barker, J. R., et al. 2011, Chemical Kinetics and Photochemical Data for use in Atmospheric Studies (Evaluation No. 17; Pasadena, CA: JPL)
Schmidt, J. A., Johnson, M. S., & Schinke, R. 2013, PNAS, 110, 17691
Segura, A., Kasting, J. F., Meadows, V., et al. 2005, AsBio, 5, 706
Segura, A., Meadows, V. S., Kasting, J. F., et al. 2007, A&A, 472, 665
Selsis, F., Despois, D., & Parisot, J.-P. 2002, A&A, 388, 985
Sonntag, C., & von Gunten, R. 2012, Chemistry of Ozone in Water and Wastewater Treatment: From Basic Principles to Applications (London: IWA Publishing)
Tian, F., France, K., Linskey, J. L., et al. 2014, E&PSL, 385, 22
Tian, F., & Ida, S. 2015, NatGe, 8, 177
Walker, J. C. G., Turekian, K. K., & Hunten, D. M. 1970, JGR, 75, 3558
West, A. A., Hawley, S. L., Walkowicz, L. M., et al. 2004, AJ, 128, 426
WMO (World Meteorological Organization) 1985, Atmospheric Ozone Assessment of our Understanding of the Process Controlling its Present Distribution and Change, Vol. 3, WMO Report No. 16 (Geneva: WMO)
Woolley, H. W. 1954, JRNBS, 52, 289
Yung, Y. L., & DeMore, W. B. 1999, Photochemistry of Planetary Atmospheres (New York, NY: Oxford Univ. Press)
Zahnle, K., Haberle, R. M., Catling, D. C., et al. 2008, JGR, 113, E11004